All Chemical Vapor Deposition Growth of MoS_2:h-BN Vertical van der Waals Heterostructures

Shanshan Wang,[1] Xiaochen Wang,[1] Jamie H. Warner[1]*

[1]Department of Materials, University of Oxford, Parks Road, Oxford, OX1 3PH, United Kingdom

Email: Jamie.warner@materials.ox.ac.uk

Abstract

Vertical van der Waals heterostructures are formed when different 2D crystals are stacked on top of each other. Improved optical properties arise in semiconducting transition metal dichalcogenide 2D materials, such as MoS_2, when they are stacked onto the insulating 2D hexagonal Boron Nitride. Most work to date has required mechanical exfoliation of at least one of the TMDs or h-BN materials to form these semiconductor:insulator structures. Here, we report a direct all-CVD process for the fabrication of high quality monolayer MoS_2:h-BN vertical heterostructured films with isolated MoS_2 domains distributed across 1cm. This is enabled by the use of few-layer h-BN films that are more robust against decomposition than monolayer h-BN during the MoS_2 growth process. The MoS_2 domains exhibit different growth dynamics on the h-BN surfaces compared to bare SiO_2, confirming there is strong interaction between the MoS_2 and underlying h-BN. Raman and photoluminescence spectroscopies of CVD-grown MoS_2 are compared to transferred MoS_2 on both types of substrates our results show directly-grown MoS_2 on h-BN films have smaller lattice strain, lower doping level, cleaner and sharper interfaces and high quality interlayer contact.

Rapid progress in the research of two-dimensional (2D) atomic crystals, such as graphene, monolayer and multilayer hexagonal boron nitride (h-BN) and transition metal dichalcogenides (TMDCs), has extended to the fabrication of vertical heterostructures with different types of 2D crystals stacking on top of each other. The flexible and transparent heterostructures compiled by van der Waals stacking of various 2D materials produces novel heterojunctions that have great potential in electronic and optoelectronic applications.[1–5] The layer-by-layer heterostructures were first created by stacking different types of materials through sequential mechanical transfer techniques.[1] However, this method is complicated with several disadvantages, such as the contamination at the interface, the low quality of interlayer contact, the high requirements on the position control for different 2D crystals stacking on top of each other, and the lack of future scalable production for large area coverage.[1,6–8] The direct growth of vertical layered heterostructures *via* chemical vapour deposition (CVD) is much more promising in terms of scalability. Recent advances have demonstrated that vertical heterostructures, such as graphene/h-BN,[9] MoS_2/graphene,[10] $MoSe_2$/graphene,[11] MoS_2/h-BN,[12] WS_2/h-BN[13], MX_2/SnS_2 (M=Mo, W, X=S, Se)[14] and WS_2/MoS_2,[8] can be grown by CVD. Growing 2D materials on h-BN exploits the advantage that h-BN has an atomically flat surface without dangling bonds and charged impurities, as well as being chemically inert, which lead to improvements in the device performance and optical properties.[15,16] However, for CVD-grown TMDCs heterostructures on h-BN substrates, there still exist challenges in utilizing CVD grown h-BN, rather than mechanically exfoliated h-BN.

h-BN obtained by mechanical exfoliation has small flake size and therefore is not possible to create large millimetre or centimetre scale heterostructured materials that could be used in large area opto-electronics like solar cells, photodetectors and 2D imaging arrays. Prior work on direct growth of MoS_2/h-BN heterostructures by CVD used organic seeding promoters to help nucleate the MoS_2 on exfoliated h-BN,[12] which might remain at the interface between MoS_2 and h-BN after growth and have some influence on the properties of this heterostructures. Ideally, a scalable approach for directly growing seed-free MoS_2 on CVD grown h-BN is needed.

There are several challenges that must be overcome in order to successfully grow a TMD on h-BN by an all-CVD approach. Firstly, the h-BN grown on Cu by CVD needs to be transferred to an alternative substrate, because of the S will react the Cu. The transfer of CVD grown h-BN films from Cu to TMDC growth compatible substrates like $Si:SiO_2$ or sapphire must be clean, with the polymer scaffold used for transfer removed to leave an exposed h-BN surface for direct growth of TMDCs. The growth temperature should not be too high, because this will increase the decomposition of the h-BN film before the TMD has been grown. This suggests that the lower growth temperature of MoS_2 compared to WS_2 is preferred. The process should be hydrogen-free, as the introduction of H_2 gas at high temperature will decompose the h-BN film. Residual oxygen in the CVD system, and oxygen species available from the metal-oxide precursor commonly used to grow TMDCs is likely to also etch the h-BN during the CVD growth of TMDCs.

Results and discussion
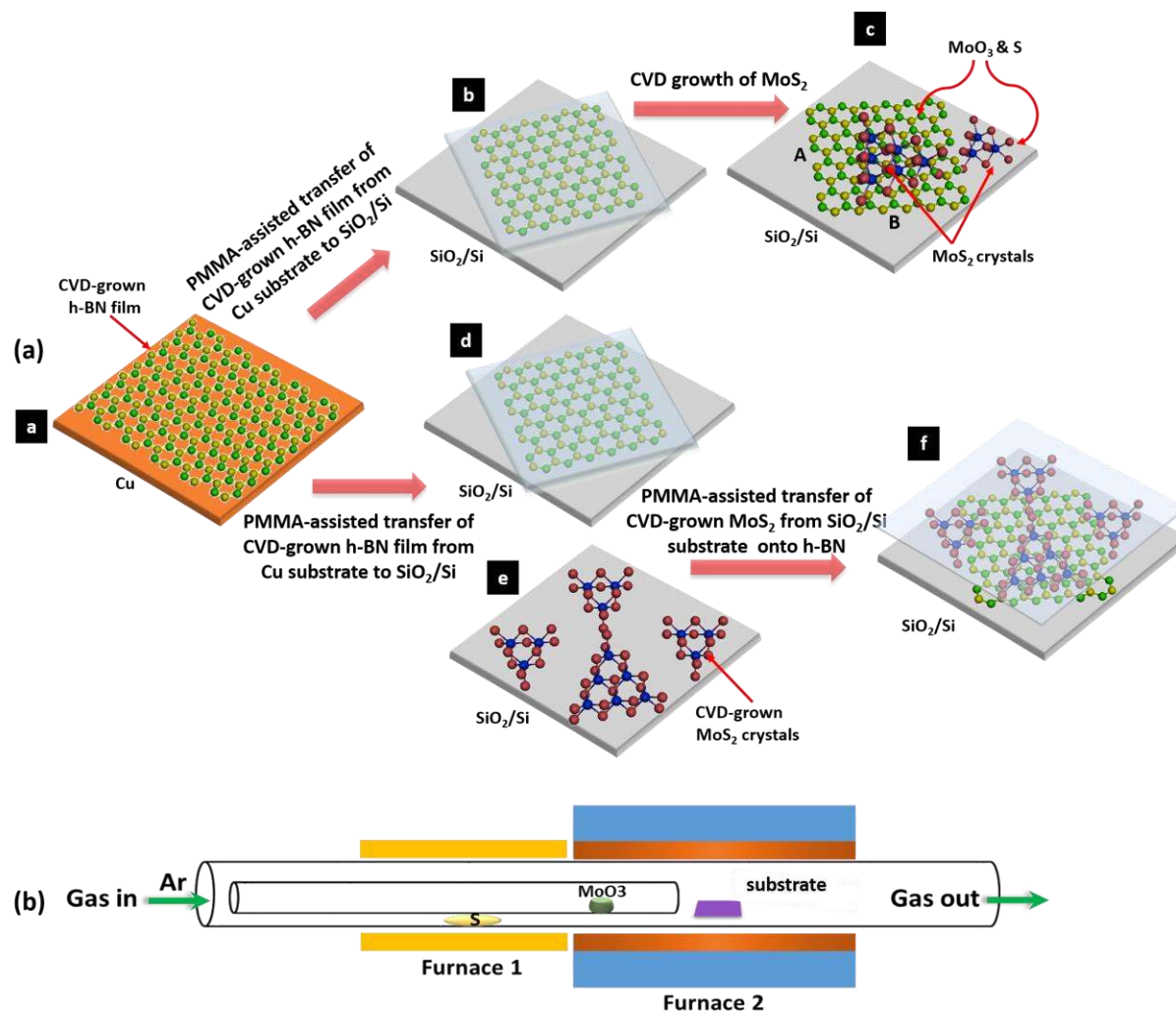
Figure 1. (a) A schematic illustration of two fabrication process of MoS_2/h-BN heterostructures. The first method is initially transferring the CVD-grown h-BN film from a copper foil to the center of a SiO_2/Si chip, leaving four corners of the substrate to be bare SiO_2 surface. Then load this substrate with face up into the CVD system to grow MoS_2 on it. The MoS_2 domains will cover both h-BN and SiO_2 areas. The second approach is through a two-step PMMA-assisted transfer process. The CVD-grown h-BN film was still first transferred onto the center of a SiO_2/Si chip surface, followed by stacking another layer of CVD-grown MoS_2 domains on the whole substrate surface, making us obtain transferred MoS_2 domains on h-BN in the central area and on SiO_2 at four corners. Two of the

transfer boundaries of h-BN film on the SiO_2 surface in the first fabrication method is labeled by the letters of A and B, respectively. (b) A schematic illustration of the CVD system for MoS_2 growth.

2D MoS_2 crystals are grown on the substrate of CVD-grown h-BN film under atmospheric pressure using MoO_3 (molybdenum trioxide) and sulphur powder as precursors. When we attempted to grow MoS_2 on monolayer h-BN films, we found that the h-BN had been substantially decomposed by the growth process and led to poor samples. Alternatively we found that using few-layer h-BN films (2-4 layers) was ideal because the films were more robust against degradation during the growth and enabled successful deposition of precursor and ultimately the growth of MoS_2 domains on a continuous few layer h-BN film. The steps of a, b and c in Figure 1(a) present the fabrication process of the MoS_2/h-BN vertical heterostructures by CVD. The few layer h-BN film was initially grown on the Cu substrate by CVD using an ammonia borane precursor, and then transferred onto the central area of a bare SiO_2/Si chip by a PMMA-assisted method, leaving four corners of the substrate as bare SiO_2 surfaces. The PMMA was removed by acetone to leave a clean h-BN. The substrate with h-BN was subsequently loaded into the CVD system designed for the growth of 2D MoS_2 on the top of both h-BN film and SiO_2. In order to compare the differences between directly growing MoS_2 on h-BN by CVD method with those fabricated by a transfer process, as seen in the steps of a, d, e and f in Figure 1a, we also did MoS_2/h-BN heterostructures *via* a two-step PMMA-assisted transfer approach. This involved replacing the direct CVD synthesis of MoS_2 (step c) with another transfer process of the CVD-grown 2D MoS_2 crystals from the original Si chip to a new SiO_2/Si substrate having h-BN film covered in the center and SiO_2 exposed at four corners (step e and f). For the CVD system of MoS_2 growth, as depicted in Figure 2b, two separated furnaces were used to realize better temperature control on both precursors and the substrate. Six hundred milligrams of

sulphur powder and the substrate were put in the center of furnace 1 and 2, respectively, where the temperature can be independently controlled. MoO_3 powder was loaded in the upstream of the second furnace, where the heating temperature can be adjusted by changing the distance between MoO_3 and the furnace center. It is noteworthy that, instead of placing two precursors in the same tube, we put 20 mg MoO_3 powder in a separated mini-tube (diameter 1 cm) inside the outer 1-inch tube, with its gas inlet loading far before the sulphur location.[17] This is to avoid any cross-contamination between sulphur and MoO_3 powder when supplying precursors into the growth area, because sulphur vapor can react with solid state MoO_3 at its evaporation temperature (~300°C) in our experiment and decrease its amount, leading to the attenuation of MoO_3 evaporation rate, and thus resulting in an unstable precursor supply in vapor phase. The substrate, having CVD-grown h-BN films pre-transferred onto the central area, was placed horizontally in the center of the second furnace, which enables us to compare the 2D MoS_2 growth on different substrates. Typical growth temperatures used for sulphur, MoO_3 and the substrate are ~180°C, ~300°C and ~800°C, respectively. Sulphur powder was pre-heated before increasing the temperature of MoO_3 to ensure the sufficient supply of sulphur vapor in the growth system. The detailed growth recipe and a brief introduction about the 'pulse-style' precursor supply mode used in our experiment is provided in the Supporting Information. This simple, scalable CVD growth approach can realize the direct fabrication of large area MoS_2/h-BN heterostructures with a clean interface and good interlayer contact, which is advantageous over mechanical transfer method.
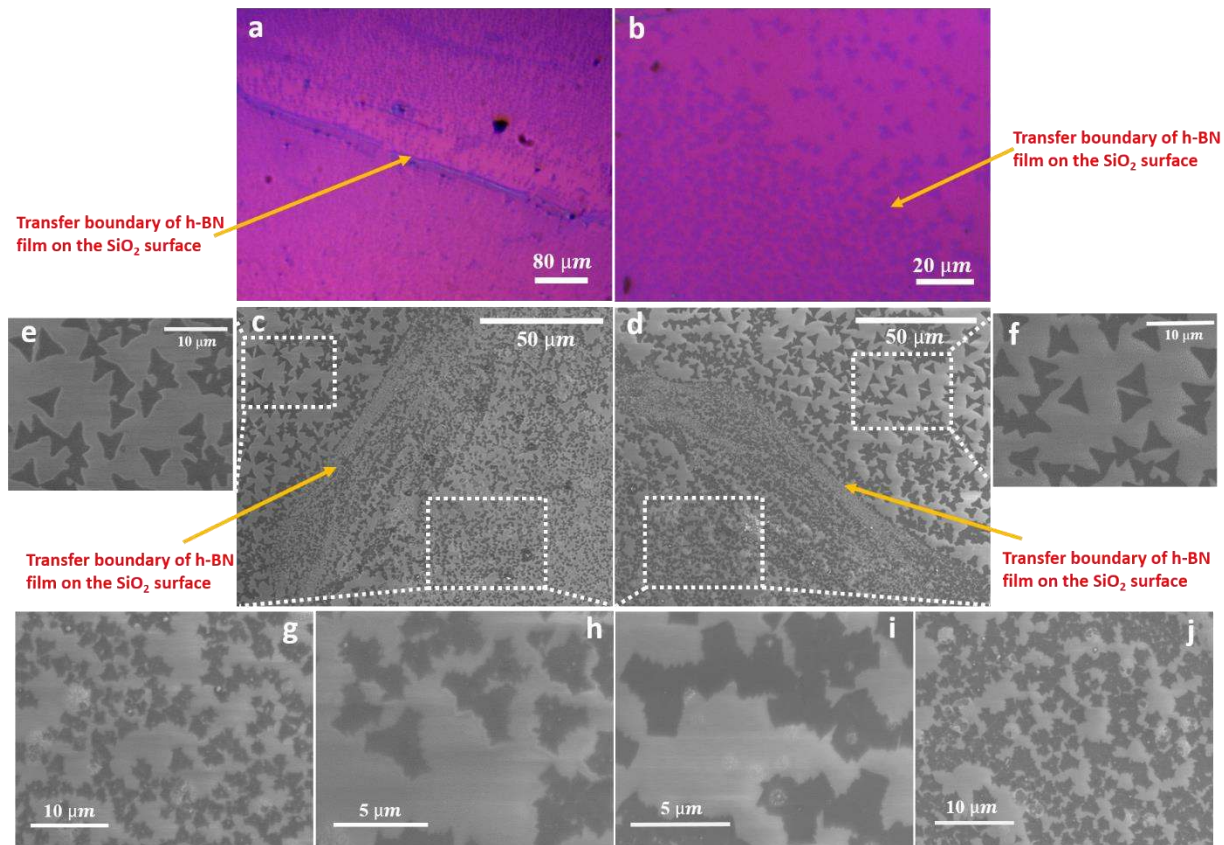
Figure 2. (a and b) Optical microscopy images of the edge region of the h-BN film on the SiO_2 surface, showing MoS_2 crystals grown by CVD both on and off the h-BN film. (c and d) SEM images of CVD-grown MoS_2 crystals grown around the edge region of the h-BN film on the SiO_2 surface marked by letters of A and B, respectively, in step C of Figure 1a. (e and f) Zoomed in SEM images of MoS_2 crystals grown on the SiO_2 in the region of white boxes shown in Figure 2c and 2d, respectively. (g-j) Zoomed in SEM images of MoS_2 crystals grown on the h-BN film in the region of white boxes shown in Figure 2c and 2d, respectively.

Figure 2a and b are optical microscope (OM) images around the transfer boundary of h-BN on SiO_2 showing 2D MoS_2 growth occurs over a large area. The homogeneous color contrast of MoS_2 domains indicates the thickness uniformity. The 2D MoS_2 crystals grown on the h-BN film exhibit a pronounced higher nucleation density and smaller domain size, compared to those grown on the SiO_2, which may result from the higher roughness of transferred h-BN film on SiO_2 (Figure S1(c) of the Supporting Information). The small optical contrast from the h-BN

film on SiO_2 can be attributed to its negligible opacity in the visible spectrum arising from its large band gap (>5 eV), making it hard to be detected.[18] However, the existence of h-BN under 2D MoS_2 has been confirmed by Raman spectroscopy, which will be discussed afterwards. The SEM images (Figure 2c-j) displays more detailed information, such as the variations of MoS_2 crystal morphology on different substrates. It can be seen that, MoS_2 crystals grown on SiO_2 are not exact triangles with sharp edges as normally observed, but rather are three-pointed star shaped with an average domain size of ~5 µm. For those grown on h-BN, the crystal shape transforms to truncated three-point stars with a flake size decrease to ~3 µm. We interpret the formation of three-point-star-shaped instead of triangular domains of MoS_2 on SiO_2 to the ultra-low Mo:S ratio of precursors absorbed on the substrate, and attribute the crystal shape and size difference between MoS_2 on h-BN and on SiO_2 to the growth rate and time variations arising from different interactions between precursor species and two types of substrate surface (Figure S2 of the Supporting Information).[19]
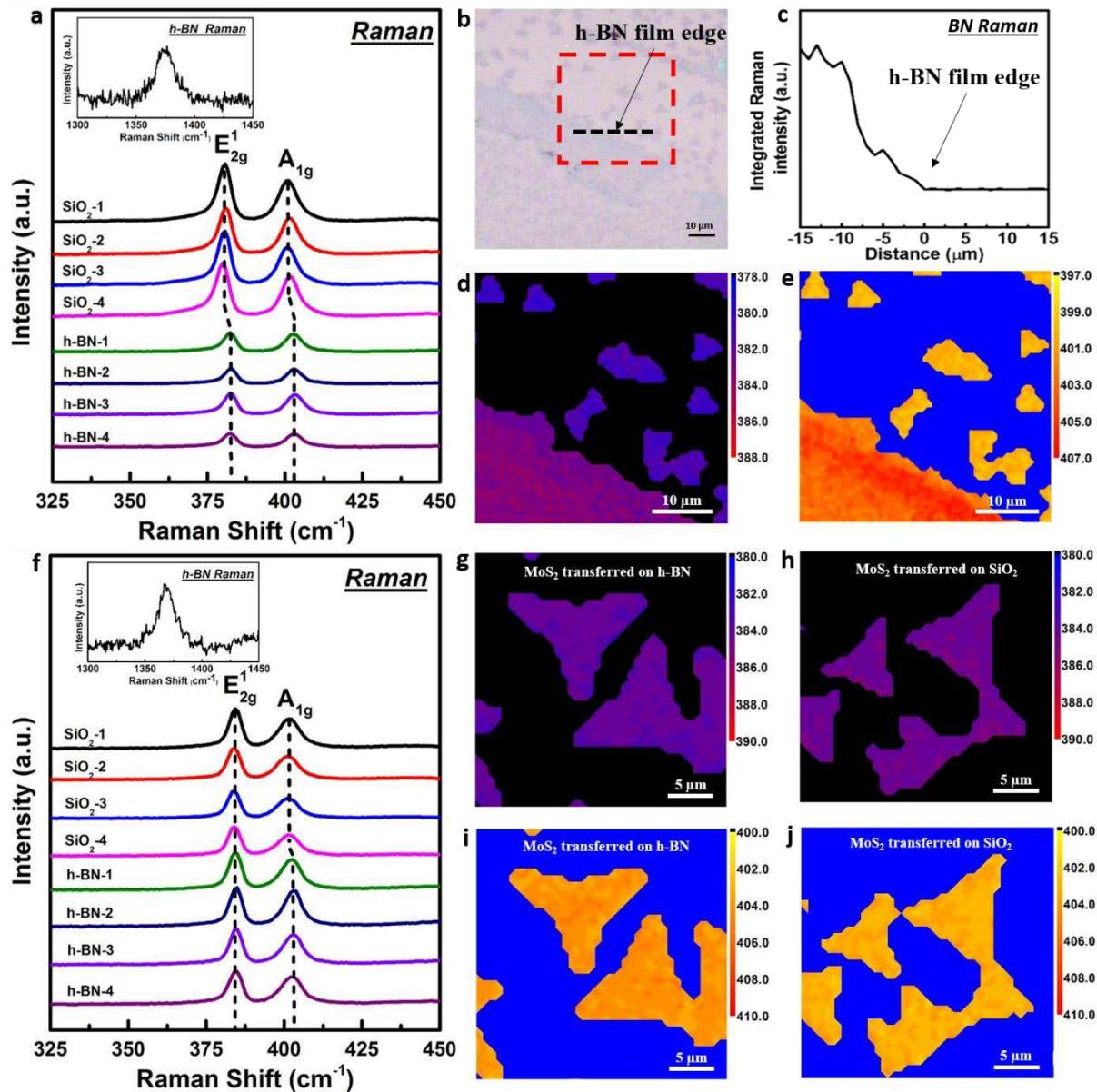
Figure 3. (a) Raman spectra collected from eight different MoS_2 domains grown on two types of substrate, four of which are grown on the SiO_2 surface, another four are grown on the h-BN film. The inset shows the Raman spectra measured from the h-BN film under the directly grown MoS_2 crystals. (b) An optical image showing the MoS_2 crystal growth around the region of the transferred h-BN film edge. (c) A plot of the integrated h-BN Raman peak intensity as a function of distance, which was measured across the edge of the h-BN film, marked by a black dashed line in Figure 3b. The point on the curve which is indicated by a black arrow corresponds to the location of the h-BN film edge in Figure 3b, as the integrated h-BN Raman peak disappears from this point. (d and e) Raman maps of direct-grown MoS_2 domains on different substrates, plotting the spatial variation of the peak position for E^1_{2g} and

A_{1g} mode, respectively, in the area of the red box marked in Figure 3b, where the upper right region has the substrate of SiO_2 and the left bottom area has the substrate of h-BN. (f) Raman spectra collected from eight different MoS_2 domains transferred on two types of substrate, four of which are transferred on the SiO_2 surface, another four are transferred on the h-BN film. The inset shows the Raman spectra measured from the h-BN film under the transferred MoS_2 crystals. (g-j) Raman maps of the peak position for E^1_{2g} and A_{1g} mode, respectively, of transferred MoS_2 domains on different substrates, h-BN and SiO_2.

Raman spectroscopy is a very useful technique to determine the layer number of MoS_2 by measuring the frequency difference between two characteristic vibration modes, E^1_{2g} and A_{1g}.[20,21] The E^1_{2g} mode represents the in-plane vibration of molybdenum and sulphur atoms, while the A_{1g} mode is related to the out-of-plane vibration of sulphur atoms.[21] Figure 3a shows the Raman spectrums of the direct-grown MoS_2 on CVD-grown h-BN film and on SiO_2, respectively, with an excitation wavelength of 532nm. The fitting results show that, for MoS_2 grown on h-BN, these two modes are centered at ~380.6 cm^{-1} and 401.2 cm^{-1}, respectively, while those MoS_2 domains grown on SiO_2 have these two vibration modes located at ~382.4 cm^{-1} and ~402.9 cm^{-1}, respectively, both giving a frequency difference of ~20.5 cm^{-1}. This is compatible with the CVD-grown monolayer MoS_2 in previous works.[12,22,23] The inset of Figure 3a is the measured characteristic Raman peak of CVD-grown h-BN under MoS_2 domains, which is located at ~1372 cm^{-1}, confirming the existence of the h-BN film after experiencing the growth process of MoS_2. A line scan was also carried out, measuring the Raman spectrum point-by-point for the characteristic h-BN vibration mode across a transfer boundary of h-BN film on SiO_2, marked by the dashed black line in Figure 3b. Figure 3c shows a plot of the integrated h-BN Raman peak as a function of distance, and it rapidly disappears in the central region. It confirms that this region is the edge of the transferred h-BN film on SiO_2 and figures 3d and 3e are examining the boundary region.

We also observed peak location variations of both modes, when MoS$_2$ were grown on different substrates. In Figure 3a, compared to the Raman spectra of MoS$_2$ grown on SiO$_2$, a pronounced phonon mode stiffening reflected with the blue-shift of both E$^1_{2g}$ and A$_{1g}$ peaks can be observed for MoS$_2$ grown on h-BN. The variations are measured to be ~1.8 cm^{-1} and 1.7 cm^{-1} for E$^1_{2g}$ and A$_{1g}$ mode, respectively. We also performed Raman mappings around the region of a transfer boundary, where half of the mapping area had the monolayer MoS$_2$ grown on the h-BN film and another half had MoS$_2$ on SiO$_2$ (Figure 3b). By plotting the 2D spatial variation of the magnitude of E$^1_{2g}$ and A$_{1g}$ peak frequency separately (Figure 3d and e), it can be found that the frequency difference for these two characteristic vibration modes depending on the growth substrate is ubiquitously observed on the sample. Furthermore, we also investigated the substrate effect on transferred CVD-grown MoS$_2$ domains on these two types of material, h-BN film and SiO$_2$, *via* a two-step PMMA-assisted transfer method (steps A, D, E and F in Figure 1a). It was found that both of the MoS$_2$ on h-BN and on SiO$_2$ had the E$^1_{2g}$ peak centred at almost the same wavenumber, while the A$_{1g}$ mode of MoS$_2$ on h-BN appeared a slight blue-shift in a value of ~0.7 cm^{-1}, compared to that of MoS$_2$ on SiO$_2$ (Figure 3f). This phenomena can also be commonly observed on the sample by comparing the Raman mapping of frequencies for these two characteristic modes of MoS$_2$ on h-BN and on SiO$_2$, respectively (Figure 3g-j). The inset of Figure 3g shows the characteristic Raman vibration mode of the h-BN film lying underneath the transferred MoS$_2$ domains, which is measured to be at ~1368 cm^{-1}.

In addition to distinguishing the number of layers, Raman spectra can also be utilized to investigate other effects such as lattice strain, doping levels and the van der Waals interaction at the interface for 2D crystals.[24–30] The in-plane Raman mode, E$^1_{2g}$, is sensitive to the built-in strain of 2D MoS$_2$,[25–27,29] and therefore, the E$^1_{2g}$ peak position variation of ~1.8 cm^{-1} observed in

Figure 3a can be attributed to the different strain effect in monolayer MoS_2 grown on h-BN and on SiO_2. In order to determine the MoS_2 lattice strain on these two types of substrates, we used the same growth method to produce MoS_2 on a bare SiO_2/Si substrate followed by measuring its Raman spectra, and then transferred these MoS_2 domains onto another SiO_2/Si substrate, and measured the Raman spectra again. The transfer process is aimed at releasing the potential strain existing in the direct-grown MoS_2 crystals. It was found that the E^1_{2g} mode of transferred MoS_2 crystals showed a blue-shift of 1.7-2.0 cm^{-1}, compared to the direct-grown ones on SiO_2, while the A_{1g} peak position remained unchanged (Figure S4 of Supporting Information). Given that the Gruneisen parameter of E^1_{2g} mode is 0.54,[31] we determined that the monolayer MoS_2 crystals grown on SiO_2 suffered a biaxial lattice tensile strain of ~0.45%, in agreement with the previous reports on CVD grown monolayer MoS_2 on the same substrate.[25] Considering that the monolayer MoS_2 grown on h-BN has a ~1.8 cm^{-1} blue-shift of E^1_{2g} mode, which is quite similar to the frequency variation (1.7-2.0 cm^{-1}) between the strain-free transferred MoS_2 and the direct grown MoS_2 on SiO_2, it indicates that using the CVD-grown h-BN film as a substrate can lead to a much smaller lattice strain in monolayer MoS_2 grown above, which may arise from the weak van der Waals force at the interface of MoS_2/h-BN heterostructures, making the lattice strain easier to release. This conclusion is further supported by the negligible frequency difference of E^1_{2g} mode between transferred monolayer MoS_2 located on h-BN and on SiO_2, indicating that E^1_{2g} mode is barely affected by other factors, such as substrate materials, doping levels, interlayer contact, *etc.*, except for the built-in strain. In terms of A_{1g} mode, which is associated with the doping level, a stiffening of it in a value of ~1.7 cm^{-1} for MoS_2 grown on h-BN film, compared with that on SiO_2 can be attributed to the reduced electron density in monolayer MoS_2.[32,33] Compared with SiO_2, h-BN is known to have a much lower degree of charged impurities, which

can decrease the doping level of the above 2D MoS_2, since there will be less charge transfer from the substrate to MoS_2 through the interface, being consistent with recent studies.[34–36] The A_{1g} peak frequency difference between MoS_2 on h-BN and on SiO_2 drastically decreases from ~1.7 cm^{-1} to ~0.7 cm^{-1}, when this contact mode is realized by the transfer process instead of direct growth. As aforementioned, there is no change on the A_{1g} peak position between the direct-grown and the transferred monolayer MoS_2 on SiO_2/Si. This means that, through the transfer process, the blue-shift magnitude of A_{1g} mode for MoS_2 on h-BN obviously reduces. This could result from two reasons, one is the contamination from different kinds of solvents used during transfer, which spoil the clean interface and increase the doping effect,[33] another possible reason is the lower quality of interlayer interaction between monolayer MoS_2 and the h-BN film underneath, which may arise from the higher surface roughness of CVD-grown h-BN film transferred on SiO_2/Si, compared with the bare SiO_2/Si surface.[26]

However, as the laser-induced thermal effect can change the anharmonicity in the lattice potential energy of MoS_2, having an influence on both E^1_{2g} and A_{1g} mode, [26,37,38] one may argue that, in our experiment, the shift could also be produced by a laser-induced temperature contribution. In order to exclude any thermal effects, we set all the experimental conditions used in each Raman measurement to be constant, so that the thermal effect would be approximately the same for different samples. Furthermore, we did a comparison experiment by decreasing the acquisition time from 2s to 0.5s accompanied by a reduction on the number of spectra averaged for signal to noise enhancement from 2 to 1, it was found that there was no obvious shift on the position of both E^1_{2g} and A_{1g} peak (Figure S5 of Supporting Information), which indicates that the laser-induced thermal perturbation in our experiment can be ignored.

The peak intensity as well as the intensity ratio between A_{1g} and E^1_{2g} also show slight differences for MoS$_2$ on different substrates. For transferred samples, the Raman intensity for both vibration modes of MoS$_2$ on h-BN appears stronger with a slightly higher intensity ratio of A_{1g}/E^1_{2g}, compared to that of MoS$_2$ on SiO$_2$ (Figure 3g and h). This could arise from the substrate-induced interference effects, as the absorption and the emission intensities can be strongly modulated by the interference within different types of substrates.[24] However, for the direct-grown MoS$_2$ on BN, even though the A_{1g}/E^1_{2g} intensity ratio is still higher than that of the direct-grown MoS$_2$ on SiO$_2$, in agreement with the phenomenon observed in the transferred samples, the intensities of both characteristic modes decrease drastically. This could possibly be due to two reasons. One is the smaller MoS$_2$ domain size, which makes the precise focus of laser spots onto MoS$_2$ crystals under optical microscope to be more difficult. The other reason is the higher roughness of monolayer MoS$_2$ domains grown on h-BN film, since the contact quality between the direct-grown MoS$_2$ and h-BN film is higher than the transferred one, making the directly grown MoS$_2$ conform to the rougher landscape of the transferred h-BN film underneath. The lower quality of the laser beam focus as well as the fluctuation of the domain surface could both result in the decrease of the signal intensity for a confocal Raman apparatus.
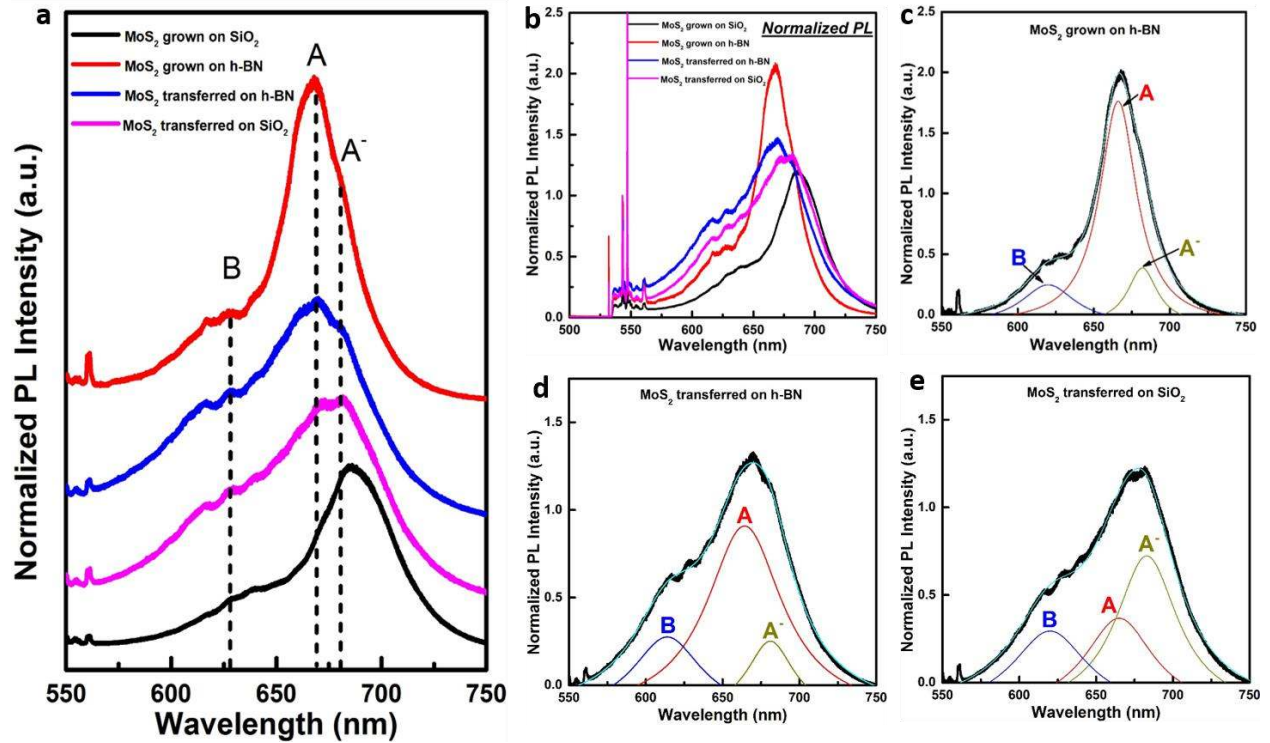
Figure 4. (a) PL spectra of the direct-grown and transferred MoS_2 on h-BN and SiO_2, respectively, which highlights the peak shape and location variation. The dashed black lines indicate the positions of three main peak emissions, B excitonic transition (B), the neutral excitonic transition of A (A) and the charged excitonic transition of A (A^-), which can be easily found in the PL of strain-free MoS_2 domains, including the direct-grown MoS_2 on h-BN and the transferred MoS_2 on either h-BN or SiO_2. (b) PL spectra of the direct-grown and transferred MoS_2 on h-BN and on SiO_2, respectively, normalized by the MoS_2 Raman intensity to highlight the PL intensity variation. (c-e) Fits to the PL peak of strain-free MoS_2 with three sub-peaks corresponding to A, A^- and B, respectively.

Next, we investigate the photoluminescence (PL) of monolayer MoS_2 in different conditions. The PL spectra is normalized against the Raman intensity to show the relative luminescence quantum efficiency between different samples.[20] As depicted in Figure 4a, for the PL spectra of transferred MoS_2 on either h-BN or SiO_2 and the direct-grown MoS_2 on h-BN, which are proved to be almost strain-free in the lattice, there are mainly three sub-peaks, located at ~625 nm, ~670 nm and ~680 nm, respectively, which constitute the whole PL spectra of MoS_2. It is known that, for intrinsic monolayer MoS_2, two pronounced PL peaks located at ~670 nm (A

peak) and ~625 nm (B peak), respectively, can be observed.[27,20] The peak of A is due to the neutral exciton emission from the direct transition at the K point, and the B peak arises from exciton emission from another direct transition between the conduction band and a lower lying valence band. However, the MoS_2 is easy to be unintentionally negatively doped, when it is contaminated with some types of solvent, or is just placed on SiO_2, which provides a relatively high level of trapped donors on the surface.[33,39] Then, a third peak, located at lower energy than A peak, emerges, and it can be associated with the recombination of negatively charged excitons of A (trions, A^-), that is, a free electron bound to a neutral exciton *via* Coulomb interaction. Compared with the literature data, the observed three sub-peaks in our PL for strainless MoS_2 correspond to the aforementioned B, A and A^- excitonic transition modes, respectively.[24,36,40,41] The energy difference between A and A^-, which is ~30 meV, arises from the large binding energy of the second electron in A^-.[40] We further extract quantitative information of three types of strainless MoS_2 by fitting the data to Lorentzian functions with three peaks located at wavelengths corresponding to B, A and A^- excitonic species (Figure 4c to e). The results show a difference in integrated PL intensity ratio between A and A^- (A/A^-), indicating that the relative populations of neutral to charged A excitons is affected by the doping level of MoS_2. The higher the doping level is, the lower this ratio will be. It was found that the MoS_2 directly grown on h-BN has the highest A/A^-, followed by transferred MoS_2 on h-BN with transferred MoS_2 on SiO_2 being the lowest. This observation further reveals the high degree of charged impurities for SiO_2, in agreement with the study on Raman A_{1g} mode above, and the contaminations introduced *via* transfer process, which can also increase the doping level of MoS_2, making the transferred MoS_2 have a significantly lower A/A^- than the direct grown one even on the same substrate material of h-BN film. Moreover, in Figure 4a, for direct-grown MoS_2 on SiO_2, its PL peak corresponding to

the direct transition at the K point experiences a redshift to ~686 nm, leading it to be in an even lower energy than the A$^-$ transition mode of the strain-free MoS$_2$. We interpret the PL softening phenomenon as a signature of the tensile strain existence in MoS$_2$ lattice, which is well compatible with the analysis of Raman E$^1_{2g}$ mode aforementioned and other recent studies, because it has been reported that a uniaxial tensile strain can not only affect Raman modes but also reduce the band gap of monolayer MoS$_2$, leading to a redshift on its A excitonic transition mode.[27]

As seen in Figure 4b, the direct-grown MoS$_2$ on h-BN has a stronger PL intensity with narrower FWHM (full width at haft maximum) than both transferred samples and direct-grown MoS$_2$ on SiO$_2$, indicating the higher crystallinity of the direct-grown MoS$_2$ on h-BN with a clean interface and a lower level of charged impurities. It is worth noting that the PL intensity of transferred MoS$_2$ on h-BN and on SiO$_2$ is similar, which means the substrate of h-BN does not show obvious advantage to SiO$_2$ when the contact between MoS$_2$ domains and substrates is realized through the transfer process instead of direct CVD growth. This could be due to the heavy doping effects on MoS$_2$ from solvent contaminations in the transfer, which covers up the superiority of the low charged impurity level of h-BN compared with SiO$_2$. This phenomenon further highlights the merits of using CVD approach to fabricate such MoS$_2$/h-BN heterostructures.

Conclusions

In summary, we have demonstrated the fabrication of high quality MoS$_2$/h-BN vertical van der Waals heterostructures through the direct CVD growth of monolayer MoS$_2$ on h-BN films. We utilized large area h-BN films grown by CVD on copper, which are then transferred onto the SiO$_2$/Si substrates. Based on the analysis of Raman and PL spectra, we found that the

direct CVD-grown MoS_2 crystals on h-BN film suffered smaller lattice strain and lower doping levels than those directly grown on SiO_2. This led to a higher percentage of exciton recombination compared to trion recombination. In addition, this direct vapour phase growth of MoS_2/h-BN heterostructures also had reduced contamination and better interlayer interactions at the interface, compared to those obtained *via* layer-by-layer polymer assisted transfer methods. This direct and versatile fabrication approach of MoS_2/h-BN heterostructures may have potential in electronic and optoelectronic applications and open up the possibility to create other types of TMDCs/h-BN heterostructures.

Methods

CVD growth of MoS₂:h-BN

The multilayer h-BN films was grown on the copper foil (Cu, 25µm, Alfa Aesar) with the precursor of ammonia borane (≥97%, Sigma Aldrich) using atmospheric pressure CVD (APCVD). The growth was carried out under the temperature of 1,000°C for 40 minutes with argon and hydrogen mixed gas, while the ammonia borane powder was heated up to ~80°C. The as-grown multilayer h-BN films was then transferred onto the central area of a bare SiO_2/Si chip, which was subsequently used as the substrate to grow monolayer MoS_2. The synthesis of 2D MoS_2 occurred with the precursors of molybdenum trioxide (MoO_3, ≥99.5%, Sigma Aldrich) and sulphur (S, ≥99.5%, Sigma Aldrich) in APCVD using argon as carrier gas. S powder was loaded in the outer 1-inch quartz tube at the central area of furnace 1, while MoO_3 was placed in the mini-tube at the upstream of furnace 2, being ~1-2 cm away from its left open. The substrate was put with face up in the center of furnace 2. After flushing the system for 60 min with argon, S vapor was pre-introduced into the growth region for 15 min by heating furnace 1 to 180°C. Then the temperature of the second furnace was increased to ~800°C in a speed of 40°C/min and kept

for 15 minutes under 150 sccm (standard cubic centimeters per minute) argon flow, and at the same time the location where MoO_3 powder was placed reached a temperature of ~300°C. Next, the argon flow rate was reduced to 10 sccm and maintained for 25 minutes, followed by a fast cooling process. More detailed CVD growth procedure for multilayer h-BN films and 2D MoS_2 on h-BN was provided in the supporting information.

Raman and PL characterization

Raman and PL spectra, including corresponding mappings are measured using a JY Horiba LabRAM ARAMIS imaging confocal Raman microscope under a laser excitation wavelength of 532 nm with a power of ~2 mW at room temperature. The spot size of the laser is ~1 µm. For the measurement of MoS_2 spot spectra, the acquisition time is 2 seconds with the accumulation to be twice. For the measurement of Raman mapping, the acquisition time is 0.1 seconds for each spot with a step size of ~0.8 µm. When measuring h-BN film, the acquisition time is 30 seconds with the number of spectra averaged to be 1. The step size of the h-BN Raman map is ~1 µm.

Reference

(1)   Geim, A. K.; Grigorieva, I. V. Van der Waals Heterostructures. *Nature* **2013**, *499*, 419–425.

(2)   Britnell, L.; Gorbachev, R. V; Jalil, R.; Belle, B. D.; Schedin, F.; Mishchenko, A.; Georgiou, T.; Katsnelson, M. I.; Eaves, L.; Morozov, S. V; *et al.* Field-Effect Tunneling Transistor Based on Vertical Graphene Heterostructures. *Science* **2012**, *335*, 947–950.

(3)   Georgiou, T.; Jalil, R.; Belle, B. D.; Britnell, L.; Gorbachev, R. V; Morozov, S. V; Kim, Y.-J.; Gholinia, A.; Haigh, S. J.; Makarovsky, O.; *et al.* Vertical Field-Effect Transistor Based on Graphene-WS_2 Heterostructures for Flexible and Transparent Electronics. *Nat. Nanotechnol.* **2013**, *8*, 100–103.

(4)   Yu, W. J.; Liu, Y.; Zhou, H.; Yin, A.; Li, Z.; Huang, Y.; Duan, X. Highly Efficient Gate-Tunable Photocurrent Generation in Vertical Heterostructures of Layered Materials. *Nat. Nanotechnol.* **2013**, *8*, 952–958.

(5)   Cheng, R.; Li, D.; Zhou, H.; Wang, C.; Yin, A.; Jiang, S.; Liu, Y.; Chen, Y.; Huang, Y.; Duan, X. Electroluminescence and Photocurrent Generation from Atomically Sharp WSe_2/MoS_2 Heterojunction p-n Diodes. *Nano Lett.* **2014**, *14*, 5590–5597.

(6)   Kretinin, A. V; Cao, Y.; Tu, J. S.; Yu, G. L.; Jalil, R.; Novoselov, K. S.; Haigh, S. J.; Gholinia, A.; Mishchenko, A.; Lozada, M.; *et al.* Electronic Properties of Graphene Encapsulated with Different Two-Dimensional Atomic Crystals. *Nano Lett.* **2014**, *14*, 3270–3276.

(7)   Haigh, S. J.; Gholinia, A; Jalil, R.; Romani, S.; Britnell, L.; Elias, D. C.; Novoselov, K. S.; Ponomarenko, L. A; Geim, A K.; Gorbachev, R. Cross-Sectional Imaging of Individual Layers and Buried Interfaces of Graphene-Based Heterostructures and Superlattices. *Nat. Mater.* **2012**, *11*, 764–767.

(8)   Gong, Y.; Lin, J.; Wang, X.; Shi, G.; Lei, S.; Lin, Z.; Zou, X.; Ye, G.; Vajtai, R.; Yakobson, B. I.; *et al.* Vertical and In-Plane Heterostructures from WS_2/MoS_2 Monolayers. *Nat. Mater.* **2014**, *13*, 1135–1142.

(9)   Liu, Z.; Song, L.; Zhao, S.; Huang, J.; Ma, L.; Zhang, J.; Lou, J.; Ajayan, P. M. Direct Growth of Graphene/Hexagonal Boron Nitride Stacked Layers. *Nano Lett.* **2011**, *11*, 2032–2037.

(10)   Shi, Y.; Zhou, W.; Lu, A.-Y.; Fang, W.; Lee, Y.-H.; Hsu, A. L.; Kim, S. M.; Kim, K. K.; Yang, H. Y.; Li, L.-J.; *et al.* Van der Waals Epitaxy of MoS_2 Layers Using Graphene as Growth Templates. *Nano Lett.* **2012**, *12*, 2784–2791.

(11)   Shim, G. W.; Yoo, K.; Seo, S.-B.; Shin, J.; Jung, D. Y.; Kang, I.-S.; Ahn, C. W.; Cho, B. J.; Choi, S.-Y. Large-Area Single-Layer $MoSe_2$ and Its van der Waals Heterostructures. *ACS Nano* **2014**, *8*, 6655–6662.

(12)   Ling, X.; Lee, Y.; Lin, Y.; Fang, W.; Yu, L.; Dresselhaus, M. S.; Kong, J. Role of the Seeding Promoter in MoS_2 Growth by Chemical Vapor Deposition. *Nano Lett.* **2014**, *14*, 464–472.

(13)   Okada, M.; Sawazaki, T.; Watanabe, K.; Taniguch, T.; Hibino, H.; Shinohara, H.; Kitaura, R. Direct Chemical Vapor Deposition Growth of WS_2 Atomic Layers on Hexagonal Boron Nitride. *ACS Nano* **2014**, *8*, 8273–8277.

(14)   Zhang, X.; Meng, F.; Christianson, J. R.; Arroyo-Torres, C.; Lukowski, M. A.; Liang, D.; Schmidt, J. R.; Jin, S. Vertical Heterostructures of Layered Metal Chalcogenides by van der Waals Epitaxy. *Nano Lett.* **2014**, *14*, 3047–3054.

(15)   Dean, C. R.; Young, A. F.; Meric, I.; Lee, C.; Wang, L.; Sorgenfrei, S.; Watanabe, K.; Taniguchi, T.; Kim, P.; Shepard, K. L.; *et al.* Boron Nitride Substrates for High-Quality Graphene Electronics. *Nat. Nanotechnol.* **2010**, *5*, 722–726.

(16)   Gannett, W.; Regan, W.; Watanabe, K.; Taniguchi, T.; Crommie, M. F.; Zettl, A. Boron Nitride Substrates for High Mobility Chemical Vapor Deposited Graphene. *Appl. Phys. Lett.* **2011**, *98*, 242105.

(17)   Zhang, J.; Yu, H.; Chen, W.; Tian, X.; Liu, D.; Cheng, M.; Xie, G.; Yang, W.; Yang, R.; Bai, X.; *et al.* Scalable Growth of High-Quality Polycrystalline MoS_2 Monolayers on SiO_2 with Tunable Grain Sizes. *ACS Nano* **2014**, *8*, 6024–6030.

(18)   Gorbachev, R. V; Riaz, I.; Nair, R. R.; Jalil, R.; Britnell, L.; Belle, B. D.; Hill, E. W.; Novoselov, K. S.; Watanabe, K.; Taniguchi, T.; *et al.* Hunting for Monolayer Boron Nitride: Optical and Raman Signatures. *Small* **2011**, *7*, 465–468.

(19)   Wang, S.; Rong, Y.; Fan, Y.; Pacios, M.; Bhaskaran, H.; He, K.; Warner, J. H. Shape Evolution of Monolayer MoS_2 Crystals Grown by Chemical Vapor Deposition. *Chem. Mater.* **2014**, *26*, 6371-6379

(20)   Splendiani, A.; Sun, L.; Zhang, Y.; Li, T.; Kim, J.; Chim, C.-Y.; Galli, G.; Wang, F. Emerging Photoluminescence in Monolayer MoS_2. *Nano Lett.* **2010**, *10*, 1271–1275.

(21)   Tonndorf, P.; Schmidt, R.; Böttger, P.; Zhang, X.; Börner, J.; Liebig, A.; Albrecht, M.; Kloc, C.; Gordan, O.; Zahn, D. R. T.; *et al.* Photoluminescence Emission and Raman Response of Monolayer MoS_2, $MoSe_2$ and WSe_2. *Opt. Express* **2013**, *21*, 4908–4916.

(22)   Najmaei, S.; Liu, Z.; Zhou, W.; Zou, X.; Shi, G.; Lei, S.; Yakobson, B. I.; Idrobo, J.-C.; Ajayan, P. M.; Lou, J. Vapour Phase Growth and Grain Boundary Structure of Molybdenum Disulphide Atomic Layers. *Nat. Mater.* **2013**, *12*, 754–759.

(23)   Wang, X.; Feng, H.; Wu, Y.; Jiao, L. Controlled Synthesis of Highly Crystalline MoS$_2$ Flakes by Chemical Vapor Deposition. *J. Am. Chem. Soc.* **2013**, *135*, 5304–5307.

(24)   Buscema, M.; Steele, G. A.; van der Zant, H. S. J.; Castellanos-Gomez, A. The Effect of the Substrate on the Raman and Photoluminescence Emission of Single-Layer MoS$_2$. *Nano Res.* **2014**, *7*, 1–11.

(25)   Liu, K.; Yan, Q.; Chen, M.; Fan, W.; Sun, Y.; Suh, J.; Fu, D.; Lee, S.; Zhou, J.; Tongay, S.; *et al.* Elastic Properties of Chemical-Vapor-Deposited Monolayer MoS$_2$, WS$_2$, and Their Bilayer Heterostructures. *Nano Lett.* **2014**, *14*, 5097–5103.

(26)   Zhou, K.; Withers, F.; Cao, Y.; Hu, S.; Yu, G.; Casiraghi, C. Raman Modes of MoS$_2$ Used as Fingerprint of Van der Waals Interactions. *Nano Lett.* **2014**, *8*, 9914–9924.

(27)   Conley, H. J.; Wang, B.; Ziegler, J. I.; Haglund, R. F.; Pantelides, S. T.; Bolotin, K. I. Bandgap Engineering of Strained Monolayer and Bilayer MoS$_2$. *Nano Lett.* **2013**, *13*, 3626–3630.

(28)   Rice, C.; Young, R.; Zan, R.; Bangert, U.; Wolverson, D.; Georgiou, T.; Jalil, R.; Novoselov, K. Raman-Scattering Measurements and First-Principles Calculations of Strain-Induced Phonon Shifts in Monolayer MoS$_2$. *Phys. Rev. B* **2013**, *87*, 081307.

(29)   Hui, Y. Y.; Liu, X.; Jie, W.; Chan, N. Y.; Hao, J.; Hsu, Y.-T.; Li, L.-J.; Guo, W.; Lau, S. P. Exceptional Tunability of Band Energy in a Compressively Strained Trilayer MoS$_2$ Sheet. *ACS Nano* **2013**, *7*, 7126–7131.

(30)   Yang, L.; Cui, X.; Zhang, J.; Wang, K.; Shen, M.; Zeng, S.; Dayeh, S. a; Feng, L.; Xiang, B. Lattice Strain Effects on the Optical Properties of MoS$_2$ Nanosheets. *Sci. Rep.* **2014**, *4*, 5649.

(31)   Cai, Y.; Lan, J.; Zhang, G.; Zhang, Y.-W. Lattice Vibrational Modes and Phonon Thermal Conductivity of Monolayer MoS$_2$. *Phys. Rev. B* **2014**, *89*, 035438.

(32)   Chakraborty, B.; Bera, A.; Muthu, D. V. S.; Bhowmick, S.; Waghmare, U. V; Sood, A. K. Symmetry-Dependent Phonon Renormalization in Monolayer MoS$_2$ Transistor. *Phys. Rev. B* **2012**, *85*, 161403.

(33)   Mao, N.; Chen, Y.; Liu, D.; Zhang, J.; Xie, L. Solvatochromic Effect on the Photoluminescence of MoS$_2$ Monolayers. *Small* **2013**, *9*, 1312–1315.

(34)   Bao, W.; Cai, X.; Kim, D.; Sridhara, K.; Fuhrer, M. S. High Mobility Ambipolar MoS$_2$ Field-Effect Transistors: Substrate and Dielectric Effects. *Appl. Phys. Lett.* **2013**, *102*, 042104.

(35)   Mos, T.; Ghatak, S.; Pal, A. N.; Ghosh, A. Nature of Electronic States in Atomically Thin MoS$_2$ Field-Effect Transistors. *ACS Nano* **2011**, *5*, 7707–7712.

(36) Tongay, S.; Zhou, J.; Ataca, C.; Liu, J.; Kang, J. S.; Matthews, T. S.; You, L.; Li, J.; Grossman, J. C.; Wu, J. Broad-Range Modulation of Light Emission in Two-Dimensional Semiconductors by Molecular Physisorption Gating. *Nano Lett.* **2013**, *13*, 2831–2836.

(37) Sahoo, S.; Gaur, A. P. S.; Ahmadi, M.; Katiyar, R. S. Temperature-Dependent Raman Studies and Thermal Conductivity of Few-Layer MoS_2. *J. Phys. Chem. C* **2013**, *117*, 9042–9047.

(38) Najmaei, S.; Liu, Z.; Ajayan, P. M.; Lou, J. Thermal Effects on the Characteristic Raman Spectrum of Molybdenum Disulfide (MoS_2) of Varying Thicknesses. *Appl. Phys. Lett.* **2012**, *100*, 013106.

(39) Lu, C.; Li, G.; Mao, J.; Wang, L.; Andrei, E. Y. Bandgap, Mid-Gap States, and Gating Effects in MoS_2. *Nano Lett.* **2014**, *14*, 4628–4633.

(40) Mak, K. F.; He, K.; Lee, C.; Lee, G. H.; Hone, J.; Heinz, T. F.; Shan, J. Tightly Bound Trions in Monolayer MoS_2. *Nat. Mater.* **2013**, *12*, 207–211.

(41) Ross, J. S.; Wu, S.; Yu, H.; Ghimire, N. J.; Jones, A. M.; Aivazian, G.; Yan, J.; Mandrus, D. G.; Xiao, D.; Yao, W.; *et al.* Electrical Control of Neutral and Charged Excitons in a Monolayer Semiconductor. *Nat. Commun.* **2013**, *4*, 1474.

TOC Graphic